ACS APPLIED ENERGY MATERIALS

Article

Cite This: ACS Appl. Energy Mater. 2019, 2, 3736−3748

www.acsaem.org

Control of Surface Defects in ZnO Nanorod Arrays with Thermally Deposited Au Nanoparticles for Perovskite Photovoltaics

Tulus,[†,‡] Selina Olthof,[§] Magdalena Marszalek,[†] Andreas Peukert,[†] Loreta A. Muscarella,[∥] Bruno Ehrler,[∥] Olivera Vukovic,[⊥] Yulia Galagan,[⊥] Simon Christian Boehme,[†] and Elizabeth von Hauff*[,†]

[†]Physics of Energy, Department of Physics & Astronomy, Faculty of Sciences, Vrije Universiteit Amsterdam, 1081 HV Amsterdam, The Netherlands

[‡]Laboratory of Technology for Polymer, Agency for the Assessment and Application of Technology (BPPT), Jakarta 10340, Indonesia

[§]Institute of Physical Chemistry, University of Cologne, Cologne 50937, Germany

[∥]Center for Nanophotonics, AMOLF, Science Park 104, 1098 XG Amsterdam, The Netherlands

[⊥]TNO - Solliance, 5656 AE Eindhoven, The Netherlands

Supporting Information

ABSTRACT: In this work, we employ vacuum deposited Au nanoparticles (~4 nm) to control the defect density on the surface of hydrothermally synthesized ZnO nanorod arrays (ZnO-NR), which are of interest for electron-transport layers in perovskite solar cells. Using a combination of photoluminescence spectroscopy, X-ray photoelectron spectroscopy, and ultraviolet photoelectron spectroscopy, we show that the Au particles reduce the presence of defects in the ZnO-NR. We discuss this in terms of trap filling due to band bending at the ZnO-NR surface. As a proof-of-concept, we apply the Au-decorated ZnO-NR as electron-transport layers in mixed-cation and mixed-halide lead perovskite solar cells ($Cs_{0.15}FA_{0.85}PbI_{2.75}Br_{0.25}$). Devices prepared with the Au-decorated ZnO-NR electron-transport layers demonstrate higher open-circuit voltages and fill factors compared to solar cells prepared with pristine ZnO-NR, resulting in an increase in the power-conversion efficiency from 11.7 to 13.7%. However, the operational stability of the solar cells is not improved by the Au nanoparticles, indicating that bulk properties of the perovskite may limit device lifetime.

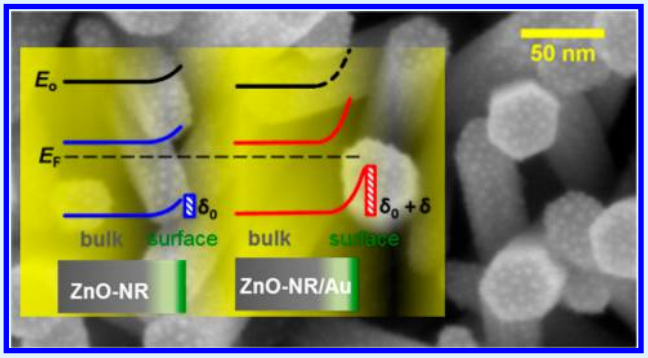

KEYWORDS: *transport layer, ZnO nanostructures, perovskite photovoltaics, mixed cation, mixed halide, interface, defects, photoelectron spectroscopy*

I. INTRODUCTION

Perovskite photovoltaics has seen unprecedented progress in reported power-conversion efficiencies since 2009.[1−3] Perovskites used in photovoltaics have the crystal structure of ABX_3, where A is a cation (such as methylammonium (MA, $CH_3NH_3^+$), formamidinium (FA, $CH_3(NH_2)_2^+$), Cs^+, or Rb^+), B is a divalent metal ion (such as Pb^{2+}or Sn^{2+}), and X is a halide (such as I^-, Br^-, or Cl^-).[3−7] Recent breakthroughs in efficiency have been achieved with mixed-cation and mixed-anion perovskites.[3−8] Besides perovskite composition, device interfaces are widely recognized as a bottleneck for both efficiency and stability.[6,9−13] In particular, recent reports have highlighted the need for developing high-performance electron-transport layers (ETL)[14,15] to reduce interfacial recombination losses that ultimately limit solar-cell efficiency.[16,17]

The use of ZnO as an ETL for emerging thin-film photovoltaics offers a wide range of potential advantages. ZnO is a wide bandgap semiconductor with high electron mobility, with reported values of 200−300 $cm^2\ V\ s^{-1}$ for bulk material and ~1000 $cm^2\ V\ s^{-1}$ for single-crystal nanowires[18−20] and suitable energy levels for efficient extraction of electrons.[21,22] Despite these advantages, ZnO is currently not widely used in perovskite solar cells[23−27] compared to other n-type metal oxides, such as, for example, TiO_2, SnO_2, and NiO_x,[26−29] likely because of issues of decomposition of the perovskite film in first generation ZnO/$MAPbI_3$ structures.[30,31] Additionally, the complex nature of crystal defects in ZnO

Received: March 2, 2019
Accepted: April 26, 2019
Published: April 26, 2019

DOI: 10.1021/acsaem.9b00452
ACS Appl. Energy Mater. 2019, 2, 3736−3748

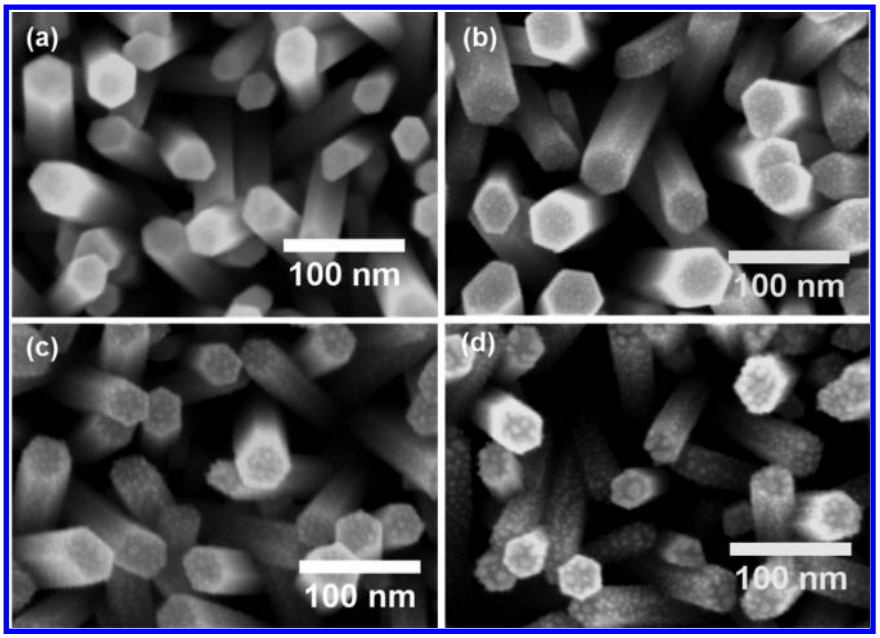

Figure 1. Top-view SEM images of (a) ZnO nanorods (ZnO-NR), (b) 0.4 nm Au-decorated ZnO nanorods (ZnO-NR/0.4Au), (c) 0.8 nm Au-decorated ZnO nanorods (ZnO-NR/0.8Au), and (d) 1.2 nm Au-decorated ZnO nanorods (ZnO-NR/1.2Au).

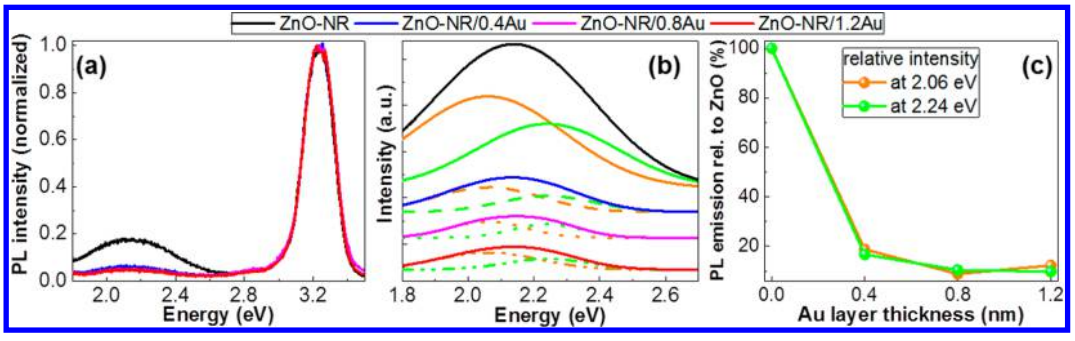

Figure 2. (a) PL spectra of the ZnO-NR (black solid line), ZnO-NR/0.4Au (blue solid line), ZnO-NR/0.8Au (pink solid line), and ZnO-NR/1.2Au (red solid line). (b) Zoom of (a), the defect PL region, where each data set has been fit with two Gaussian distributions, one centered at 2.24 eV (green lines, corresponding to the "green luminescence" in ZnO) and one centered at 2.06 eV (orange lines, corresponding to the "orange luminescence" in ZnO). Fits of the ZnO-NR, ZnO-NR/0.4Au, ZnO-NR/0.8Au, and ZnO-NR/1.2Au are shown as solid, dashed, dotted, and dashed dotted lines, respectively. Traces were plotted with vertical offsets to enhance clarity. (c) The PL emission relative to the ZnO-NR substrate at 2.06 eV (orange) and at 2.24 eV (green) as a function of Au coverage.

films and nanostructures has generally limited its application in optoelectronic devices.[21,32]

Decorating ZnO with Au nanoparticles is an intriguing strategy to both passivate the prominent surface defects in ZnO and to increase light absorption in the solar-cell active layer via near-field plasmonic enhancement or light scattering.[33−37] Some publications have demonstrated that decorating ZnO nanostructures with Au nanoparticles quenches green emission from defect states in the ZnO while simultaneously increasing photocatalytic activity.[37−45] However, the underlying mechanisms and electronic interactions between ZnO and Au are not well-understood.[37,46,47]

Here we investigate the influence of Au nanoparticles on the surface defects and properties of ZnO-NR. These ZnO-NR are prepared via chemical bath deposition, whereas the Au nanoparticles are subsequently formed by thermally evaporating Au onto the ZnO-NR, resulting in small (∼4 nm), evenly distributed Au nanoparticles. The deposition of Au particles via thermal deposition, instead of wet chemical methods, reduces unwanted chemical residue on the ZnO surface. Using photoluminescence (PL) spectroscopy, we find that Au-decorated ZnO-NR (ZnO-NR/Au) exhibit a decreased emission from surface defects compared to pristine ZnO-NR. This is in excellent agreement with observations from impedance spectroscopy and X-ray photoelectron spectroscopy (XPS), which show a reduction in the density of trap states at the ZnO-NR/Au/perovskite interface and a reduction in surface defect density, respectively. Finally, UV photoelectron spectroscopy (UPS) correlates these results with an increase in band bending at the ZnO-NR surface because of Au, leading to the effective filling of these surface states. As a proof-of-concept, we test the performance of mixed-cation and mixed-halide lead perovskite solar cells ($Cs_{0.15}FA_{0.85}PbI_{2.75}Br_{0.25}$)[48,49] prepared with ZnO-NR/Au transport layers. Solar cells prepared with ZnO-NR/Au transport layers initially show higher fill factors (FF) and open-circuit voltages (V_{oc}), leading to higher power-conversion efficiencies (PCE) than solar cells prepared with pristine ZnO-NR. However, we observe that the Au nanoparticles do not improve the operational stability of the perovskite solar cells under continuous light soaking. These

DOI: 10.1021/acsaem.9b00452
ACS Appl. Energy Mater. 2019, 2, 3736−3748

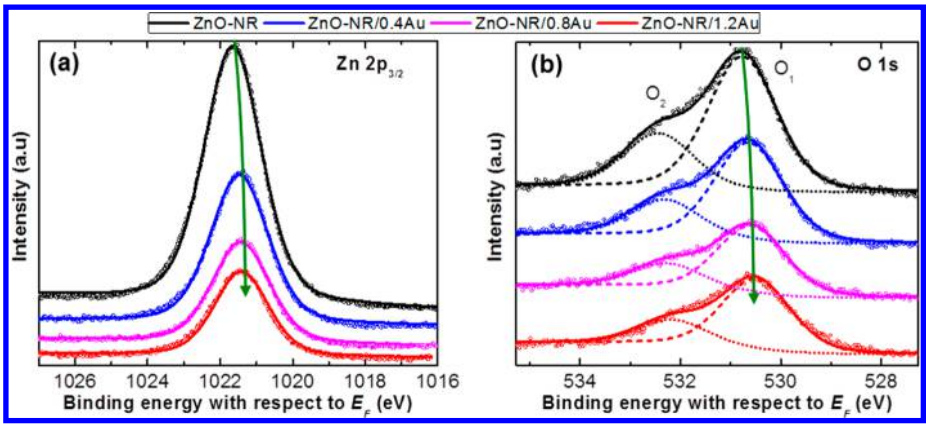

Figure 3. XPS spectra of ZnO-NR (black), ZnO-NR/0.4Au (blue), ZnO-NR/0.8Au (pink), and ZnO-NR/1.2Au (red). (a) shows the Zn $2p_{3/2}$ region, and (b) shows the O 1s region. Here, two contributions are fitted into the O 1s region: O_1 (dashed lines) represents oxygen signal from ZnO, and O_2 (dotted lines) represents surface −OH groups. Open symbols mark the measurements, whereas solid lines are fits to the data; the data sets are stacked via vertical offsets to enhance clarity.

results indicate that the operational stability of these solar cells is not only limited by defect states at the ETL interface.[27,37,46,47,50,51]

II. RESULTS AND DISCUSSION

II.i. Surface Defect Passivation in Au-Decorated ZnO Nanorods. ZnO-NR and ZnO-NR/Au samples were fabricated according to the procedure described in the Experimental Section. Briefly, ZnO-NR were deposited using chemical bath deposition (CBD) via ZnO seeding on ITO substrates.[52−54] Decoration of the ZnO-NR with Au nanoparticles was achieved by thermally depositing a thin Au layer on top of the nanorods with the sample kept at room temperature, leading to the formation of small (<10 nm) individual Au nanoparticles distributed over the ZnO-NR array. We investigated ZnO-NR/Au samples prepared with Au *effective* layer thicknesses of 0.4, 0.8, and 1.2 nm.

Figure 1(a−d) shows the top-view scanning electron microscopy (SEM) images of ZnO-NR and ZnO-NR decorated with Au at effective layer thicknesses of 0.4 nm (ZnO-NR/0.4Au), 0.8 nm (ZnO-NR/0.8Au), and 1.2 nm (ZnO-NR/1.2Au), respectively. The ZnO nanorods are 410 nm long (see Figure S1(b)), and the distribution of Au nanoparticles on the nanorod surface appears homogeneous. From the SEM images, we estimate the diameter of the Au nanoparticles to be approximately 4 ± 1.2 nm, and we cannot identify differences in the Au nanoparticle size between the samples.

Figure 2(a) shows the PL spectra of the ZnO-NR (black solid line), ZnO-NR/0.4Au (blue solid line), ZnO-NR/0.8Au (pink solid line), and ZnO-NR/1.2Au (red solid line), excited at 4.43 eV and normalized to the ZnO-NR emission at 3.23 eV (see also Figure S2(c)). The emission at around 2 eV originates from defects in the bandgap of the ZnO-NR,[50,51,55−57] and our measurements show that the relative intensity of this defect emission is lower in the ZnO-NR/Au samples compared to the ZnO-NR samples (see also Figure S2(c)). In Figure 2(b), we used two Gaussian contributions to fit the area of defect emission in the PL spectra; here the peak centers, heights, and widths were used as fitting parameters. This approach consistently yields two features, one centered at 2.06 eV (orange) (i.e., "orange emission" in ZnO) and one centered at 2.24 eV (green) (i.e., "green emission" in ZnO).[58]

Figure 2(c) shows the decrease (in percentage) of the defect emission at 2.06 eV (orange) and at 2.24 eV (green) as a function of effective Au thickness. The Au nanoparticles lead to a decrease in both green and orange emission from the ZnO by approximately 90%. Specifically, the green emission decreases by 83, 89, and 90%, and the orange emission decreases by 81, 91, and 87% for Au effective thicknesses of 0.4, 0.8, and 1.2 nm, respectively.

The intricate nature of ZnO defects has been intensively investigated in the literature.[21,32,47,55−58] Green emission is widely observed in ZnO fabricated using a variety of different protocols and is attributed to oxygen vacancies (V_o).[21,32,55,56,57,59] Orange emission, on the other hand, is commonly observed in hydrothermally synthesized ZnO and has been attributed to interstitial oxygen ions.[55−59] Our PL measurements suggest that Au nanoparticles suppressed both oxygen vacancies and interstitials.[55−59] We can infer that these defects predominantly reside at the surface, given the significant passivation by surface-bound Au nanoparticles. This is consistent with the increasing suppression of the green emission with increasing Au effective thickness.

We would like to point out that our classification of the observed defects as oxygen interstitials and oxygen vacancies is motivated by considerations of bulk ZnO.[21,32] Likely, we oversimplify the intricate nature of defects at ZnO-NR surfaces, as recent reports have suggested rich defect physics arising from surfactants, significant surface reconstructions, and concomitantly altered defect landscapes.[60,61] However, our approach is corroborated by the surprisingly similar spectral features of the defect PL of bulk ZnO and our ZnO nanorods (i.e., both exhibit the typical green and orange PL).

Next, XPS and UPS were employed to learn more about the modification of the ZnO-NR surface composition and energetics because of the Au coverage. Figure 3 shows the XPS signals of the (a) Zn $2p_{3/2}$ and (b) O 1s core levels for ZnO-NR (black), ZnO-NR/0.4Au (blue), ZnO-NR/0.8Au (pink), and ZnO-NR/1.2Au (red). The Zn $2p_{3/2}$ signals in Figures 3(a) can be well-described by a single mixed Gaussian/Lorentzian peak, indicating that Zn is present in the +2 oxidation state. The oxygen 1s signals in Figure 3(b) can be fit with two contributions, one attributed to oxygen bound in ZnO (O_1) and one attributed to surface −OH groups (O_2). First, looking at the relative peak intensities and correcting

DOI: 10.1021/acsaem.9b00452
ACS Appl. Energy Mater. 2019, 2, 3736−3748

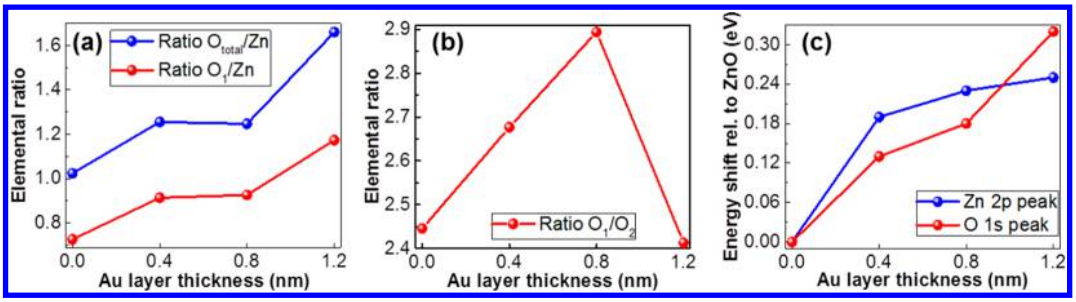

Figure 4. Values extracted from the XPS measurements for varying effective Au thicknesses of the ZnO-NR/Au samples. (a) Ratio of the peak areas of O_{total} to Zn (blue) and O_1 to Zn (red). (b) Ratio of O_1 to O_2, where O_1 represents O in ZnO, and O_2 represents surface −OH groups, respectively. (c) Relative shift of the Zn 2p (blue) and O 1s peak (red) toward lower binding energies, with respect to the ZnO-NR sample without Au.

them for their relative sensitivity factors (see Experimental Section), we can extract the elemental composition of the surface. In Figure 4(a), the ratio of the total oxygen signal (O_1 + O_2) to that of Zn is shown in blue, and the ratio between O_1 and Zn is plotted in red. We clearly observe that an increasing Au effective layer thickness leads to a relative decrease in the Zn signal with respect to the oxygen signal. The O_1 excess is increased by 26, 28, and 62% for ZnO-NR/0.4Au, ZnO-NR/0.8Au, and ZnO-NR/1.2Au, respectively, compared to O_1 excess in pristine ZnO-NR. This means that Au nanoparticles either preferably bind to the surface Zn sites, thereby covering them and rendering them unobservable, and/or induce a change in surface termination, by which the effective amount of oxygen at the surface is increased. The second scenario agrees with our finding of a decrease in defect PL, thereby supporting the hypothesis that Au leads to a reduction in surface oxygen vacancies. Figure 4(b) shows the related change in the ratio between the two different oxygen contributions, O_1/O_2 vs Au coverage. Here we observe a clear increase in the ZnO-related O_1 peak with respect to the defective OH-related O_2 up to a coverage of 0.8 nm. At this moment, it is unclear why the 1.2 nm value does not follow this trend, possibly because the gold becomes more reactive to oxygen at a certain size or the gold particles at a certain size coalesce differently.[40] More specifically, Figure 4 shows that in the case of the oxygen vacancy defects (O_1), we observe a clear trend in the reduction of defects with increasing Au coverage, whereas this trend is not as clear for the defects related to OH groups (O_2). Note that the lowest defect density in this case is found for ZnO-NR/0.8Au (highest O_1/O_2 ratio), whereas the highest is found for ZnO-NR/1.2Au. This may indicate that above a certain threshold, Au particles aggregate more strongly, possibly leaving larger areas of the surface uncovered. Our results suggest that Au deposition correlates with decreasing Zn/O excess in our nanorods. That finding would be consistent with either Au replacing (surface) Zn or attracting additional O into the ZnO lattice.

In addition, XPS can give information on the changes in Fermi level position within the band gap close to the surface, as core level peaks follow energy shifts experienced by the valence band density of states. Clear shifts are observed in the positions of the Zn- and O-related peaks, as indicated in Figure 3 by the green arrows. The respective changes in binding energy, relative to the pristine ZnO-NR substrate, are shown in Figure 4(c). Here, changes toward lower binding energy by approximately 290 ± 40 meV of the Zn 2p (blue) and O 1s (red) peaks are observed with increasing effective Au thickness.

In contrast to the strongly bound states probed by XPS, UPS gives information on the weakly bound valence band (VB) density of states (DOS), which are shown in Figure 5(a)

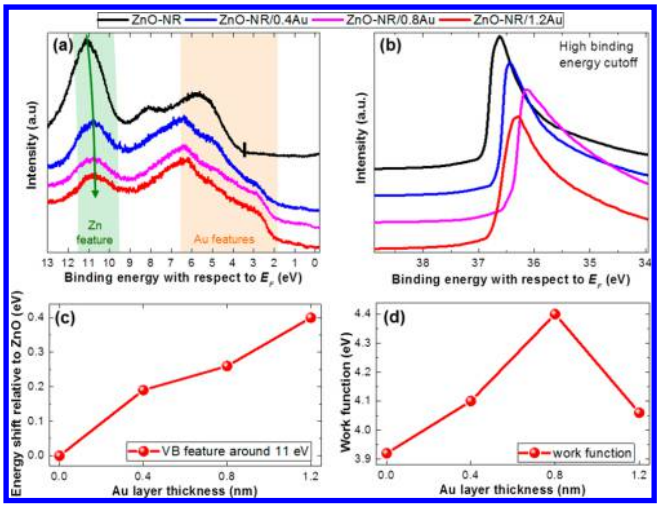

Figure 5. (a) UPS spectra of the VB regions of ZnO-NR (black solid line), ZnO-NR/0.4Au (blue solid line), ZnO-NR/0.8Au (pink solid line), and ZnO-NR/1.2Au (red solid line). The VB onset of ZnO-NR is indicated by the vertical mark at 3.45 eV, and the shift of a characteristic feature of ZnO is indicated by the green arrow. (b) Corresponding UPS spectra in the region of the high-binding-energy cutoff. The scans in (a) and (b) are offset vertically to enhance clarity. (c) Shift of the binding energy of the ZnO-related VB feature (green arrow in subfigure a) relative to the bare ZnO-NR substrate upon increasing Au coverage. (d) Change in W_f as a function of Au coverage.

measured by He II_α excitation; furthermore, the work function (W_f) can be extracted from the high-energy electron cutoff (see Figure 5(b)). Changes observed in the VB density of states with increasing Au coverage mostly originate from the growing Au contribution, which has characteristic features around 3 and 6 eV (shaded orange area). As a result of the Au DOS, the onset of the ZnO DOS cannot be read out, except in the case of zero coverage, where it is marked by a vertical black line at 3.45 eV with respect to the Fermi energy. Still, we can deduce changes induced to the ZnO-NR surface by the Au coverage using the characteristic ZnO-NR feature at 11 eV to track shifts. This feature is marked by a green arrow in Figure 5(a), and the corresponding binding-energy shift in relation to the Au coverage is plotted in Figure 5 (c). In UPS, we observe a shift to lower binding energy by 400 meV that is somewhat

DOI: 10.1021/acsaem.9b00452
ACS Appl. Energy Mater. 2019, 2, 3736−3748

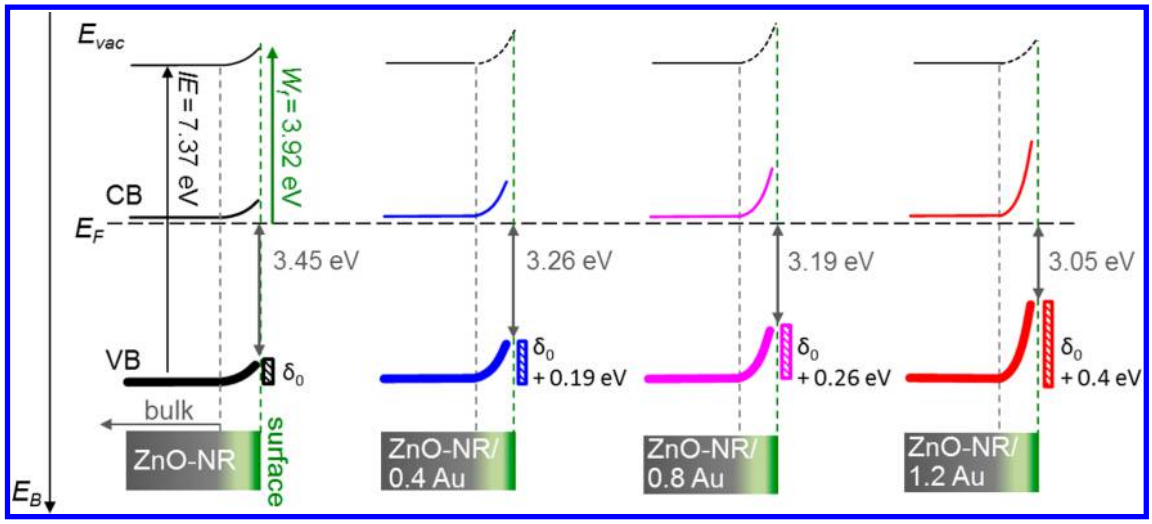

Figure 6. Schematic energy level diagrams of Au-induced band bending at the surfaces of ZnO-NR (black), ZnO-NR/0.4Au (blue), ZnO-NR/0.8Au (pink), and ZnO-NR/1.2Au (red). Shaded areas symbolize the surface band bending as observed from the UPS measurements; already for the pristine ZnO-NR sample an initial bend bending δ_0 is assumed against a not further specified bulk value, as often reported in the literature. The CB band is also included (even though not directly measured in this work) assuming a position close to the Fermi energy in the bulk. The surface work function is only stated for the pristine sample, because the value is not well-defined for the inhomogeneously Au covered samples. The ionization energy (IE) of ZnO-NR was extracted from the UPS spectra by calculating the sum of the VB onset and the W_f from Figure 5(a,b).

larger than the shift in XPS; this is expected due to the higher surface sensitivity of UPS. Finally, Figure 5(b,d) shows the high-energy cutoff as well as the extracted changes in work function, respectively. We find a monotonous increase in W_f from 3.92 to 4.4 eV up to a Au coverage of 0.8 nm; however, for the thickest Au coverage, the W_f is lowered, again indicating that the surface of that sample might have been affected by additional adsorbates.

Overall, XPS and UPS measurements both show that coverage of ZnO-NR by Au nanoparticles induces a shift of characteristic ZnO features to lower binding energies (i.e., an upward band bending of the energy levels toward the ZnO-NR surface as sketched in Figure 6). We want to note that work function values measured on the inhomogeneous Au covered surfaces should be interpreted as an "effective" W_f that is somewhere in between the low W_f of ZnO and the high W_f of Au nanoparticles.[62] Therefore, in Figure 6, we only give an indication of the trend by the dotted E_{vac} line but no actual value for the surface work function. Furthermore, we note that the band gap is not affected by Au nanoparticle coverage, as inferred from the constant energy of the PL band edge feature (see Figure 2 (a)). This suggests that the CB edge follows the same trend of upward band bending (see Figure 6).

Theoretical work on ZnO indicates that an upward shift in the Fermi level position with respect to the band edges (which corresponds to a downward shifting of the bands with respect to E_F, which is the frame of reference for the experiments here) alters the formation energies for vacancies, specifically decreasing the formation energy for Zn vacancies and increasing the formation energy for O vacancies.[32] Our UPS and XPS results consistently show that all characteristic energy levels shift to lower binding energies, corresponding to a shift of the Fermi level away from the conduction band.

Previously, ZnO nanorods have been reported to exhibit such an upward band bending at the surface (i.e., toward vacuum), for a variety of treatments,[44,55,63] which is the reason why we already indicated in Figure 6 that there might be a surface contribution δ_0 present even in the case without Au coverage. Upward band bending is equivalent to reduced n-doping at the surface[46,47] (with respect to the ZnO nanorod bulk) and may significantly alter the optoelectronic and photocatalytic properties of ZnO-based devices. For example, it has been suggested that the predominant defect species in ZnO depends on the Fermi level[21,32] and that the upward band bending creates V_o^+ sites capable of engaging in recombination processes with VB holes, yielding the typical green emission of ZnO.[55−57,59] The observed increase in this surface contribution with Au coverage in Figure 6 could have two origins: (i) the Au nanoparticles increase the upward band bending at the ZnO surface by changing the defect density of the surface and thereby the Fermi level position, or (ii) in the presence of a pre-existing surface band bending of the magnitude δ_0, the partial coverage of the ZnO by Au merely decreases the XPS and UPS probing depth. In the latter case, even unaltered band bending in Au-decorated ZnO nanorods would manifest itself as an upshift of energy levels because of increased XPS and UPS surface sensitivities. We favor interpretation (i) of the increased band bending, as interpretation (ii) cannot explain the observed quenching of the defect PL.

Our PL data (see Figure 2) suggest that coverage of the ZnO-NR with Au particles can be applied to effectively reduce the density of oxygen vacancies and defects related to OH groups on the ZnO nanorod surface. The distinct binding energies of O-containing species in XPS (see Figures 3 and 4) further allow us to conclude that Au reduces the presence of surface −OH groups. Comparing the peak areas between O_1 and O_2 (i.e., oxygen in ZnO to oxygen present as surface −OH groups, see Figure 4(b)), this ratio increases for ZnO-NR/0.4Au and ZnO-NR/0.8Au, consistent with the Au nanoparticle coverage reducing the number density of surface −OH sites. From the PL and XPS/UPS data, we cannot distinguish between the various models proposed in the literature on the charged state of the oxygen vacancy—a single-positive charge according to Barbagiovanni et al.[56,57] or the uncharged and double-positive charge according to Janotti and Van de Walle.[21,32] However, we note that it is important to account

DOI: 10.1021/acsaem.9b00452
ACS Appl. Energy Mater. 2019, 2, 3736−3748

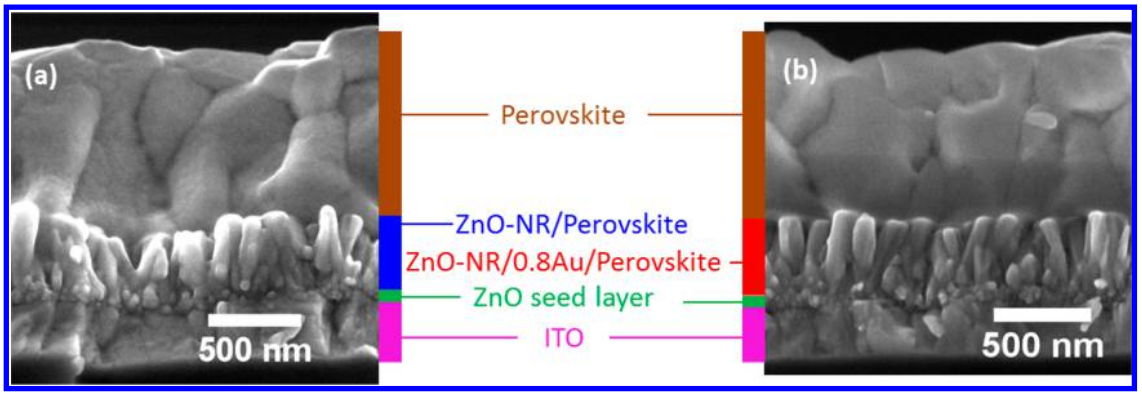

Figure 7. SEM images of perovskite deposited on ZnO-NR (a) without Au (ZnO-NR/perovskite) and (b) with 0.8 nm Au (ZnO-NR/0.8Au/perovskite).

for band bending in any case, as green defect PL can be reduced by passivating oxygen vacancies via reduced n-type character at the ZnO surface.

Previously, Au nanostructures have been reported to either quench the green emission from ZnO nanostructures, correlated with increased photocatalytic activity,[37−43] or enhance the green emission, via formation of trap states at the Au/ZnO junction induced by an upward band bending and concomitant larger depletion regions within the ZnO layer.[42,44,46,47] Our results, however, indicate that the increased upward band bending in ZnO-NR induced by Au is consistent with a reduction in defect states.[46,47]

II.ii. Perovskite-Infiltrated ZnO Nanorod Structures. We chose pristine ZnO nanorod arrays and ZnO-NR/0.8Au samples to test as an ETL in perovskite solar cells. Figure 7 shows the SEM cross sections of the perovskite layers infiltrated in the (a) ZnO-NR and (b) ZnO-NR/0.8Au samples. The samples appeared stable after thermal annealing at 100 °C for 30 min, in contrast to former reports of $MAPbI_3$ deposited onto ZnO, which was reported to quickly turn yellow, indicating a decomposition of the perovskite.[30] However, in the XRD spectra shown in Figure 8(a), we

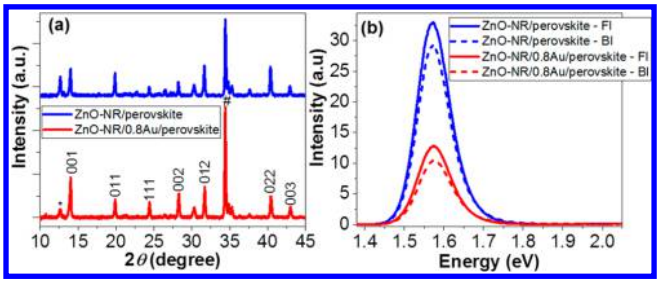

Figure 8. (a) XRD pattern of ZnO-NR/perovskite (blue solid line) and ZnO-NR/Au-0.8 nm/perovskite (red solid line); the symbol # represents the characteristic 002 peak from ZnO-NR, and the symbol * indicates the peak from PbI_2.[4] (b) PL spectra of ZnO-NR/perovskite (blue) and ZnO-NR/0.8Au/perovskite (red) under front illumination (FI, solid lines) and back illumination (BI, dashed lines), respectively.

observe that the intensity of the (001) peak of the perovskite is higher in samples containing Au nanoparticles, and furthermore, the peak at $2\theta = 12.7°$, originating from PbI_2,[4] is significantly lower here. Therefore, XRD suggests that Au suppresses the decomposition of perovskites into its constituents.

Figure 8(b) shows the PL of the ZnO-NR/perovskite (blue solid line) and the ZnO-NR/0.8Au/perovskite (red solid line) under "front illumination" (i.e., the perovskite layer faces both the excitation source and PL detector). We measured the PL spectra of the samples using an excitation wavelength of 2.64 eV to study the emission from the perovskite layer while avoiding excitation of the ZnO and Au nanoparticles. Selective excitation of the perovskite at 2.64 eV is assumed based on the absorption spectra of the perovskites (see Figure S3(b)), compared to the ZnO and Au nanoparticles (see Figure S2(b)). We normalized the perovskite PL spectra to account for slight differences in the perovskite layer thickness by dividing by the fraction of absorbed photons (F_A) at 2.64 eV, where F_A is given by

$$F_A = 1 - 10^{A} \quad (1)$$

and A is absorbance. We observe a decrease in the PL emission intensity when the absorber (see Figure S3(b)) is interfaced with ZnO and a further decrease in PL emission when Au nanoparticles are introduced in the structures.

An excitation wavelength of 2.64 eV is expected to lead to complete absorption of the excitation within the top 100 nm of the entire 800 nm perovskite layer.[64] Hence, front illumination is expected to reveal recombination processes mainly at the perovskite top surface and perovskite bulk region. To probe recombination processes at the interface with the ZnO electrode, we additionally performed experiments under "back illumination" (i.e., both the excitation light and the perovskite PL are transmitted through the glass/ITO/ZnO layers at the back of the sample). This should lead to the perovskite being excited predominantly at the ZnO interface rather than the bulk. We note, however, that the PL under back illumination (dashed lines) is only slightly less intense than under front illumination (solid lines). Although the influence of both the ZnO and the Au nanoparticles on the perovskite PL intensity is significant, the geometry of the measurement is not. We attribute the similarity in the spectra to the high diffusion lengths of charge carriers in perovskite layers. This indicates that locating defect sites in perovskite films (i.e., front surface versus bulk versus back surface of the film) with PL measurements is nontrivial.

II.iii. Impedance Modeling and Capacitance Spectra of Solar Cells. Solar cells were prepared by depositing doped spiro-OMeTAD hole-transport layers and Au electrodes onto the ZnO-NR/provskite and ZnO-NR/0.8Au/perovsite structures. Impedance spectroscopy was performed on the devices

DOI: 10.1021/acsaem.9b00452
ACS Appl. Energy Mater. 2019, 2, 3736−3748

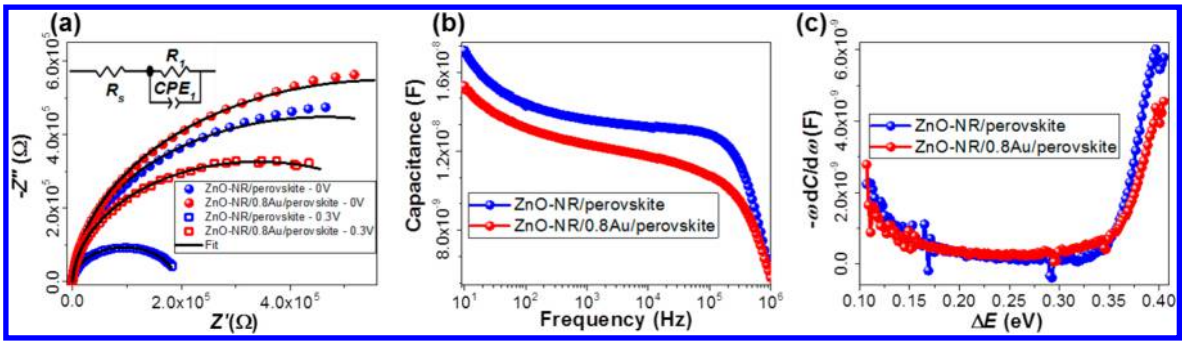

Figure 9. (a) Nyquist plot and fit of the impedance spectra from the ZnO-NR/perovskite (blue) and ZnO-NR/0.8Au/perovskite (red) devices in the dark at DC bias voltages of 0 and 0.3 V; the equivalent-circuit model (R_s−R_1CPE$_1$) in the inset was used to model the impedance spectra. (b) Capacitance−frequency (C−f) spectra of ZnO-NR/perovskite (blue) and ZnO-NR/0.8Au/perovskite (red) devices in the dark at a DC bias voltage of 0 V. (c) $-\omega\frac{dC}{d\omega}$ (t-DOS) versus ΔE of ZnO-NR/perovskite (blue) and ZnO-NR/0.8Au/perovskite (red) devices in the dark at a DC bias voltage of 0 V.

Table 1. Summary of the Values of the Circuit Elements of the Devices

sample name and DC bias voltage	R_s (Ω)	R_1 (kΩ)	Q_1 (nF)	α_1	τ (ms)
ZnO-NR/perovskite (0 V)	13.4 ± 0.1	922 ± 8	16.4 ± 0.1	0.98 ± 0.01	15
ZnO-NR/0.8Au/perovskite (0 V)	13.5 ± 0.1	1150 ± 7	16.3 ± 0.1	0.97 ± 0.01	19
ZnO-NR/perovskite (0.3 V)	13.7 ± 0.1	191 ± 1	18.4 ± 0.1	0.99 ± 0.01	4
ZnO-NR/0.8Au/perovskite (0.3 V)	13.8 ± 0.1	682 ± 4	18.3 ± 0.1	0.97 ± 0.01	12

in the dark at DC bias voltages of 0 and 0.3 V to elucidate the influence of the Au nanoparticles on the electrical properties of the ZnO/perovskite interface. Figure 9(a) shows the Nyquist plots for the ZnO-NR/perovskite (blue) and the ZnO-NR/0.8Au/perovskite (red) devices. We observe that the impedance (Z) increases with addition of Au nanoparticles. We do not observe a signature of ionic conduction, typically resulting in a low-frequency tail in the spectrum.[65]

We modeled the impedance spectra with the equivalent circuit shown in the inset of Figure 9(a). The circuit consists of a series resistance R_s to account for contacting resistance and one resistor−capacitor (R−C) element. The capacitor is modified to account for any dispersive (time-dependent) effects by introducing a constant-phase element (CPE). The impedance of the CPE (Z_{CPE}) is given by

$$Z_{CPE} = \frac{1}{Q(i\omega)^{\alpha}} \tag{2}$$

where ω is the angular frequency, Q is a coefficient, and α is a unitless parameter between 0 and 1 that accounts for dispersion in the system. If α = 1, CPE reduces to an ideal capacitor with $Q = C$, and if α = 0, the CPE reduces to an ideal resistor with $Q = 1/R$.[66]

The values for the R_1−CPE$_1$ element are very comparable at 0 and 0.3 V. We attribute this element to electrical processes at the ZnO/perovskite interface. As $\alpha \approx 1$, we set $Q = C$. Interestingly, the addition of Au nanoparticles significantly increases the resistance R_1 (922 ± 8 vs 1150 ± 7 kΩ at 0 V and 191 ± 1 vs 682 ± 4 kΩ at 0.3 V, respectively) but only minimally decreases the capacitance Q (16.4 ± 0.1 vs 16.3 ± 0.1 nF at 0 V and 18.4 ± 0.1 vs 18.3 ± 0.1 nF at 0.3 V, respectively) and decreases α (0.98 ± 0.01 vs 0.97 ± 0.01 at 0 V and 0.99 ± 0.01 vs 0.97 ± 0.01 at 0.3 V, respectively), as shown in Table 1. The time constant (τ) of the relaxation process was calculated from the time constant of the circuit, given by

$$\tau = R_1 C \tag{3}$$

If R_1 is interpreted as the recombination resistance, then τ corresponds to carrier lifetime.[67,68] ZnO-NR/Au samples yielded higher values of τ than ZnO-NR samples (15 vs 19 ms at 0 V and from 4 vs 12 ms at 0.3 V).

To gain more insight into these results, we investigate the defect distribution at the ZnO/perovskite interface. Figure 9(b) shows capacitance−frequency (C−f) spectra at DC bias voltages of 0 V in the dark for the ZnO-NR/perovskite (blue) and the ZnO-NR/0.8Au/perovskite (red) devices, respectively. We observe that adding Au results in a slight reduction in device capacitance over nearly the full frequency range, consistent with the results of the equivalent-circuit model.

To understand this more quantitatively, we examine the density of trap states (t-DOS) in the devices. By applying the approach first introduced by Walter et al.,[69,70] we investigated the t-DOS in the devices according to

$$N_T(E_\omega) = -\frac{V_{bi}}{qwk_BT}\omega\frac{dC}{d\omega} \tag{4}$$

where

$$E_\omega = k_BT\ln\left(\frac{\omega_0}{\omega}\right) \tag{5}$$

where C is the capacitance, ω is the angular frequency, ω_0 is the attempt-to-escape frequency, q is the elementary charge, k_B is Boltzmann's constant, T is the temperature, V_{bi} is the built-in potential, and w is the depletion width of the solar cell.

The model assumes that trap states located close to a characteristic demarcation energy will capture or emit charges with a characteristic frequency, thereby contributing to the frequency-dependence of the capacitance, and that the defect distribution is proportional to the derivative of device capacitance with respect to frequency. The demarcation energy is calculated from $\omega = \omega_0$ (i.e., the maximum frequency at which a defect at energy E_ω is charged or discharged by the V_{ac}

DOI: 10.1021/acsaem.9b00452
ACS Appl. Energy Mater. 2019, 2, 3736−3748

signal).[69] Features at low frequencies are attributed to shallow trap densities, and features at higher frequencies are attributed to deep trap densities.[70]

Figure 9(c) shows the plot of $-\omega\frac{dC}{d\omega}$ as a function of ΔE, where ΔE is given by

$$\Delta E = E_0 - E_\omega \quad (6)$$

and

$$E_0 = k_B T \ln(\omega_0) \quad (7)$$

, of the ZnO-NR/perovskite (blue) and the ZnO-NR/0.8Au/perovskite (red) devices. We observe that the t-DOS spectra show a deep trap state between ΔE = 0.35 eV and ΔE = 0.4 eV. The Au nanoparticles appear to reduce the density of deep traps in this energy range. We also tentatively relate these results to the larger signal from PbI_2 (see Figure 8(a)) in the ZnO-NR/perovskite device compared to the ZnO-NR/0.8Au/perovskite device (see Figure 5), in contrast to the suppressed surface defects on ZnO-NR/0.8Au (see Figure 2).

The impedance data in the dark confirm the conclusions drawn from the PL and XPS measurements: incorporation of Au nanoparticles in ZnO nanorods yields higher carrier lifetimes, lower capacitance (in agreement with the lower defect densities found in PL), and an increased resistance (possibly a fingerprint of the increased band bending inferred from XPS and UPS). Specifically, Au was found to reduce the trap density centered between 0.35 and 0.4 eV (see Figure 9(c)). As the t-DOS analysis does not discriminate between positively or negatively charged defect sites,[70] the trap density may be distributed above or below E_F in the bandgap. Depending on the nature of the trap sites and position in the bandgap, electron transfer between the Au nanoparticle and the perovskite or between the Au nanoparticle and ZnO-NR may lead to passivation of this trap density. Additionally, an increase in the E_F at the heterostructure junction under illumination would promote trap filling.

II.iv. Solar-Cell Performance. Figure 10(a) shows the current density−voltage (J−V) characteristics under illumination for the ZnO-NR/perovskite (blue) and the ZnO-NR/0.8Au/perovskite (red) devices with reverse scan (RS) at a scan rate of 182 mV/s. Generally, we observe that the ZnO-NR/0.8Au/perovskite solar cells have higher power-conversion efficiencies (PCE) than the ZnO-NR/perovskite solar cells. Specifically, devices prepared with ZnO-NR/Au vs ZnO ETL demonstrate higher open-circuit voltage (V_{oc}) and fill factor (FF) values, leading to increased PCE. The PCEs of the solar cells were observed to increase from 11.5 ± 0.2 to 12.7 ± 0.9%, the V_{oc} from 0.86 ± 0.01 to 0.92 ± 0.04 V, and the FF from 60.1 ± 0.4 to 62.8 ± 3.5% upon the addition of Au nanoparticles. The short-circuit current density (J_{sc}) of the ZnO-NR/perovskite devices is 22.1 ± 0.3 mA/cm^2, and that of the ZnO-NR/0.8Au/perovskite devices is 22.2 ± 0.1 mA/cm^2. We note that J_{sc} is not influenced by the addition of Au nanoparticles. The solar-cell parameters (taken in reverse scan) are summarized in Table 2. Figure 10(b) shows the J−V characteristics in the dark. We also observe a stark difference between the reverse scan (RS) and forward scan (FS) of the J−V characteristics of the devices (see Figure S4(b)); the addition of Au nanoparticles does not reduce the hysteresis effects. This indicates that hysteresis in the J−V of the solar cells is not related to defects in the ZnO-NR.

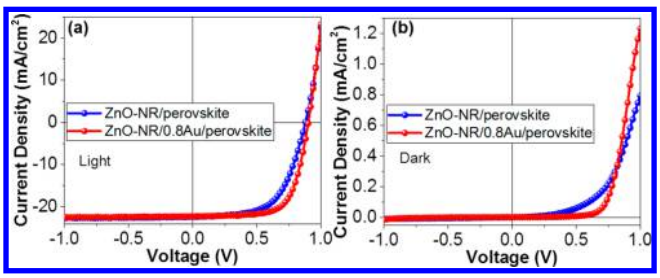

Figure 10. (a) J−V characteristics under illumination for ZnO-NR/perovskite (blue) and ZnO-NR/0.8Au/perovskite (red). (b) J−V characteristics in the dark. All measurement was performed with a reverse scan (RS) at a scan rate of 182 mV/s.

The addition of Au nanoparticles on the ZnO nanorods electrodes lead to an increase in V_{oc}, FF, and PCE of the solar cells under illumination, yet no increase in the J_{sc}, as would be expected for plasmonic enhancement. Instead, the improved PCE of the devices is consistent with reduced interfacial recombination at the electron-transport layer interface.[37,46,47,64] The increased FF and V_{oc} originate from a better diode rectification, inferred from the J−V curves in the dark (see Figure 10(b)), and point toward a critical role of defect-free electrode interfaces in photovoltaic cells. On the other hand, the typical hysteresis of perovskite solar cells seems unaffected by the presence of Au nanoparticles (see Figure S4(b)), suggesting the hysteresis to be a bulk perovskite phenomenon, at least in these devices.

II.v. Operational Stability of the Solar Cells. Figure 11 shows the time-dependent change in PCE, V_{oc}, FF, and J_{sc} of the ZnO-NR/perovskite (blue) and ZnO-NR/0.8Au/perovskite (red) devices under constant AM1.5 illumination. The performance of the ZnO-NR/0.8Au/perovskite device is initially higher but deteriorates more rapidly in these devices than for the ZnO-NR/perovskite devices. This is primarily visible in the loss of V_{oc} and FF, resulting in a decrease in PCE. In contrast, the V_{oc} of the ZnO-NR/perovskite device even increases over time, consistent with the typically observed trap filling in metal oxides under light soaking. The lack of such positive light-soaking behavior in the ZnO-NR/0.8Au/perovskite devices supports our earlier hypothesis that the surface traps are already passivated by the Au particles, as light soaking does not influence performance in these devices.

Interestingly, the Au particles appear to stabilize the J_{sc} values, leading to less relative change in J_{sc} of the ZnO-NR/0.8Au/perovskite devices compared to that of the ZnO-NR/

Table 2. Solar-Cell Parameters Obtained for Both Device Architectures from Five Devices[a]

sample name	J_{sc} (mA/cm^2)	V_{oc} (V)	FF (%)	PCE (%)
ZnO-NR/perovskite	22.1 ± 0.3 (**22.3**)	0.86 ± 0.01 (**0.88**)	60.1 ± 0.4 (**59.5**)	11.5 ± 0.2 (**11.7**)
ZnO-R/0.8Au/perovskite	22.2 ± 0.1 (**22.3**)	0.92 ± 0.04 (**0.90**)	62.8 ± 3.5 (**68.3**)	12.7 ± 0.9 (**13.7**)

[a]The error is given by the standard deviations in the parameters. The parameters of the champion cell are given in parentheses.

DOI: 10.1021/acsaem.9b00452
ACS Appl. Energy Mater. 2019, 2, 3736−3748

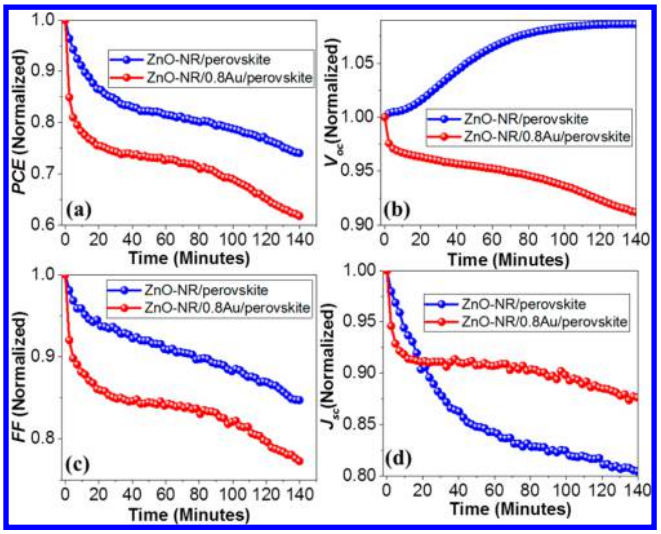

Figure 11. Change in the solar-cell parameters (a) PCE, (b) V_{oc}, (c) FF, and (d) J_{sc} during light soaking under constant illumination of the ZnO-NR/perovskite (blue) and the ZnO-NR/0.8Au/perovskite (red) devices.

perovskite devices. To investigate this behavior further, we extracted the series resistance (R_s), shunt resistance (R_{SH}), and saturation current (J_o) from the $J-V$ curves under constant illumination. Figure 12(a–c) shows the time-dependent changes in R_s, R_{SH}, and J_o. We observe that R_s increases and R_{SH} decreases under constant illumination for both device architectures. More notable is that J_o (see Figure 12(c)) increases roughly exponentially in the ZnO-NR/0.8Au/perovskite device, whereas J_o decreases roughly exponentially in the ZnO-NR/perovskite device. This behavior is consistent with the increase in V_{oc} in the ZnO-NR/perovskite device and the decrease in V_{oc} in the ZnO-NR/0.8Au/perovskite device. We do not attribute this behavior to heating of the devices during measurement, which is negligible (see Figure S7(a)). Rather, it may indicate dynamic processes of the ZnO-NR/Au/perovskite interface. We note that the phenomena in our operational stability test are nearly reversible (see Figure S7(b)) and, hence, are better described by reversible light-soaking effects than degradation processes.[46]

III. CONCLUSIONS

We demonstrate a straightforward way to control surface defects on ZnO nanorods arrays with thermally deposited Au nanoparticles. Thermal deposition of Au nanoparticles enables the formation of small, evenly distributed nanoparticles with well-defined sizes <10 nm while avoiding contamination and etching of the ZnO-NR. With a combination of PL, XPS, and UPS, we observe that the Au nanoparticles decrease the density of oxygen vacancies and OH-related surface defects in the ZnO-NR. We discuss these results in terms of Au-induced band bending in surface-near regions of the ZnO-NR. Solar cells were fabricated by infiltrating mixed-cation and mixed-halide lead perovskite ($Cs_{0.15}FA_{0.85}PbI_{2.75}Br_{0.25}$) layers into the ZnO nanorods. Impedance spectroscopy revealed a reduction in carrier recombination rates, corresponding to a reduction in the trap density in solar cells prepared with ZnO-NR/Au versus ZnO-NR transport layers. Proof-of-concept solar cells demonstrated an increase in the open-circuit voltage and fill factor and, therefore, PCE. The Au nanoparticles, however, did not increase device stability, indicating that other effects may limit device lifetime.

IV. EXPERIMENTAL SECTION

IV.i. Materials. Zinc acetate dihydrate (analysis grade) and hexamethylenetetramine (analysis grade) were purchased from Merck Chemicals and used as received. Zinc nitrate hexahydrate (reagent grade, purity 98%), cesium iodide (CsI), spiro-OMeTAD (HPLC grade, purity 99%), bis(trifluoromethane) sulfonimide lithium, chlorobenzene, ethanolamine (ACS reagent grade, purity >99%), *N*,*N*-dimethylformamide (DMF), dimethyl sulfoxide (DMSO), 4-tert-butylpyridine (purity 96%), acetonitrile, and acetone were purchased from Sigma-Aldrich and used as received. Formamidinium iodide (FAI) was purchased from Greatcell Solar (formerly Dyesol). Lead(II) iodide (PbI_2) and lead(II) bromide ($PbBr_2$) were purchased from TCI. Absolute ethanol was purchased from VWR Chemicals. Au (purity 99.99%) was purchased from Cookson Drijfhout B.V.

IV.ii. Synthesis of ZnO Nanorods by Chemical Bath Deposition. ZnO seed layers were prepared using a sol–gel method on ITO sputtered glass substrates (Praezisions Glas & Optic GmbH) with size of (25 ± 0.5) × (25 ± 0.5) mm and thickness of 1.1 ± 0.1 mm. ITO substrates were cleaned for 15 min in acetone, 15 min in ethanol, and finally 15 min in Milli-Q water (18 MΩ·cm). All cleaning steps were performed in an ultrasonic bath at room temperature. Finally, the substrates were dried by a nitrogen flux and exposed to UV/ozone (ProCleaner 220, Bioforce Nanoscience Inc.) for 15 min. For the fabrication of ZnO seeds, solution with a 0.5 M concentration of zinc acetate dihydrate and monoethanolamine (MEA) with a molar ratio of 1:1 in ethanol was prepared based on the recipe from Peukert et al.[52] The mixture was put in an ultrasonic bath at 40 °C for 20 min and was kept stirring at 40 °C for an additional 20 min. This step was repeated until a clear solution was obtained. The precursor solution was then allowed to cool to room temperature, and subsequently, 200 μL of solution was deposited on ITO glass substrate by spin-coating at 2000 rpm for 30 s. The film was then thermally annealed using a precision hot plate at 350 °C for 20 min in air.

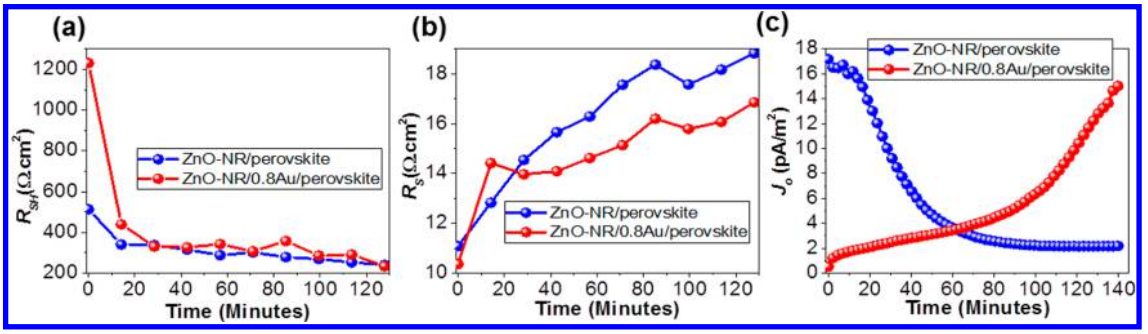

Figure 12. Change in the (a) R_{SH}, (b) R_s, and (c) J_o values during light soaking under constant illumination of the ZnO-NR/perovskite (blue) and the ZnO-NR/0.8Au/perovskite (red) devices.

DOI: 10.1021/acsaem.9b00452
ACS Appl. Energy Mater. 2019, 2, 3736–3748

ZnO-NR were subsequently prepared by deposition in a solution of 25 mM of zinc nitrate hexahydrate and 25 mM hexamethylenetetramine (molar ratio 1:1) in Milli-Q water (18 MΩ·cm).[52] The solutions were prepared according the procedure below. First, zinc nitrate hexahydrate was dissolved in half of the total volume of the solution, which was followed by ultrasonification at room temperature for 5 min. Then, hexamethylenetetramine was added to the second half of the solution, followed by ultrasonification at room temperature for 10 min and stirring on a hot plate at room temperature for 15 min. Ultrasonification was performed again for 5 min at room temperature. This was followed by stirring on the hot plate at room temperature for 15 min. ZnO-NR were grown at 80 °C for 60 min. A 20 mL aliquot of solution was used for each substrate. The samples were then cleaned by Milli-Q water and dried using N_2.

IV.iii. Deposition of Au Nanoparticles on ZnO Nanorods. To create the Au nanoparticles, a thin layer of Au was deposited on ZnO-NR in a thermal evaporation chamber at 1×10^{-6} mbar. The deposition rate was 0.1 Å/s. The recorded thicknesses of the Au were 0.4, 0.8, and 1.2 nm.

IV.iv. Preparation of Mixed-Cation and Mixed-Halide Lead Perovskite Layers. The perovskites ($Cs_{0.15}FA_{0.85}PbI_{2.75}Br_{0.25}$) were prepared using 760 mg of CsI, 2850 mg of FAI, 8259 mg of PbI_2, and 895 mg of $PbBr_2$ in 13.5 mL of DMF and 1.5 mL of DMSO. The solutions were stirred at room temperature for a few hours in a N_2 environment. The film was deposited by spin-coating 60 μL of the solution on top ZnO-NR and ZnO-NR/0.8Au at 1000 rpm for 15 s and at 5000 rpm for 45 s. After 25 s of the spin-coating process, 210 μL of chlorobenzene was sprayed on the films. Then, the films were thermally annealed at 100 °C for 30 min in a N_2 environment.

IV.v. Deposition of Doped Spiro-OMeTAD as the Hole-Transport Layer. Spiro-OMeTAD (80 mg) was dissolved in 1 mL of chlorobenzene. The solution was then stirred overnight. 4-*tert*-Butylpyridine (28.5 μL) followed by 17.5 μL of lithium bistrifluoromethanesulphonimidate solution (520 mg of lithium bistrifluoromethanesulphonimidate/1 mL of acetonitrile) were then added to the solution. The solution was then stirred for 10 min. A 50 μL aliquot of the solution was deposited on top of the perovskite layer by spin-coating at 2000 rpm for 60 s. The sample was purged in N_2 for 30 min. The samples were then exposed for at least 1 night to ambient conditions in the dark.

IV.vi. Deposition of the Au Electrode. Finally, 100 nm of Au was deposited with a rate of 1 Å/s onto the structures in a thermal evaporation chamber at 1×10^{-6} mbar.

V.vii. Photoluminescence Spectroscopy. PL measurements were performed using a Cary Eclipse − Varian B.V. in ambient conditions. Measurements on ZnO-NR and ZnO-NR/Au samples were performed with excitation at 4.43 eV (280 nm). Measurements were performed in ambient conditions with an excitation filter from 3.14 to 4.96 eV and an emission filter from 1.23 to 3.44 eV.

PL measurements on ZnO-NR/perovskite and ZnO-NR/0.8Au/perovskite structures were performed with excitation at 2.64 eV (470 nm), a scan range from 1.37 to 2.07 eV, filters for the excitation from 2.0 to 3.7 eV, and emission filters from 1.13 to 2.26 eV. The measurements were performed under both "front illumination" (with the perovskite layer facing the excitation source) and "back illumination" (via first the glass/ITO/ZnO-NR layer).

V.viii. Photoelectron Spectroscopy (XPS and UPS). The photoelectron spectroscopy measurements were performed at the Institute of Physical Chemistry, University of Cologne, Germany, in a custom-built UHV system using a Phoibos 100 hemispherical electron analyzer from Specs. The XPS was performed with an Al Kα X-ray source (VG) at an excitation energy of 1253.6 eV, whereas UPS was performed with a He plasma lamp (VG Scienta) using the He II_α line at 40.8 eV. The relative peak intensities of XPS spectra were corrected by their relative sensitivity factors (RSF, 2.93 for O and 9 for Zn).

V.ix. Impedance Spectroscopy. Impedance spectroscopy measurements were performed using a PGSTAT302N (Autolab, Metrohm) equipped with an impedance analyzer (FRA32M). The frequency range used was 1 MHz−10 Hz, and a V_{ac} amplitude of 10 mV was applied. The DC voltage was varied, and measurements were performed at 0, 0.1, 0.2, and 0.3 V in the dark.

V.x. Current−Voltage Characterization. Current−voltage curves measurements were performed in a N_2 environment. $J-V$ curves were obtained in the dark and under AM 1.5G of sun (100 mW/cm^2) illumination with a LOT solar simulator combined with a Keithley 2400 source meter controlled by a LabView program. We measured at a scan rate of 182 mV/s in the reverse scan (RS). Under illumination, a mask was used, and the effective active area was 0.16 cm^2 for these measurements. In our measurements, we employed a delay time of 50 ms between setting the voltage and reading the voltage, an integration time of 20 ms for three cycles of reading the current, a precondition voltage of 1.2 V before the start of each measurement, a hold time of 11 s, and a voltage step size of 22 mV. We also investigated the hysteresis by recording scans in both forward (FS) and reverse (RS) direction.

V.xi. Operational Stability Tests under Illumination. The operational stability tests were performed under AM 1.5G (100 mW/cm^2) illumination of a LOT solar simulator using a Keithley 2400 source meter controlled by a LabView program with a setup delay time of 50 ms, integration time of 20 ms for three cycles, precondition voltage of 1.2 V, hold time of 11 s, and voltage step size of 22 mV for the reverse scan. The measurements was performed every 2 min continuously.

■ ASSOCIATED CONTENT

Supporting Information

The Supporting Information is available free of charge on the ACS Publications website at DOI: 10.1021/acsaem.9b00452.

AFM image of ZnO seed layer; SEM images of cross section view of ZnO-NR; XRD pattern of the ZnO-NR and the ZnO-NR/0.8Au; the absorbance of the ZnO-NR and the ZnO-NR/0.8Au; absolute PL intensity of the ZnO-NR, ZnO-NR/0.4Au, ZnO-NR/0.8Au, ZnO-NR/1.2Au; XRD pattern of the perovskites on glass substrate; the absorbance and PL of the perovskites on glass substrate; the absorbance of ZnO-NR/perovskite and ZnO-NR/0.8Au/perovskite; the reverse scan (RS) and forward scan (FS) of the $J-V$ characteristics of the devices; Nyquist plots of impedance data taken from ZnO-NR/perovskite and ZnO-NR/0.8Au/perovskite devices under the dark at bias voltages of 0.1 and 0.2 V; capacitance−frequency ($C-f$) spectra, in the dark at bias voltages of 0.1, 0.2, and 0.3 V; $J-V$ curve during stability test of ZnO-NR/perovskite and ZnO-NR/0.8Au/perovskite solar cells; temperature versus time of stability test; reversibility of $J-V$ characteristics of the ZnO-NR/perovskite and the ZnO-NR/0.8Au/perovskite solar-cell devices before and after light-soaking test; details for extraction of the saturation current from the $J-V$ data (PDF)

■ AUTHOR INFORMATION

Corresponding Author

*E-mail: e.l.von.hauff@vu.nl.

ORCID

Selina Olthof: 0000-0002-8871-1549
Loreta A. Muscarella: 0000-0002-0559-4085
Yulia Galagan: 0000-0002-3637-5459
Simon Christian Boehme: 0000-0002-8399-5773
Elizabeth von Hauff: 0000-0002-6269-0540

DOI: 10.1021/acsaem.9b00452
ACS Appl. Energy Mater. 2019, 2, 3736−3748

Author Contributions

All authors contributed to the writing of the manuscript. All authors have given approval to the final version of the manuscript.

Notes

The authors declare no competing financial interest.

■ ACKNOWLEDGMENTS

The authors thank Martin Slaman, Jan Rector, Saskia Kars, Alina Chanaewa, and Leo Polak for assistance and supporting the experiments. The authors thank Rinke J. Wijngaarden and Ivan Infante for discussion. T. acknowledges the Ministry of Research, Technology and Higher Education, the Republic of Indonesia for the scholarship Program for Research and Innovation in Science and Technology (RISET-Pro) World Bank Loan No. 8245-ID. T., E.v.H., and Y.G. acknowledge the COST Action Stable Next Generation Photovoltaics (Grant No. MP1307) for support. S.C.B. acknowledges The Netherlands Organization of Scientific Research (NWO) for financial support through the Innovational Research Incentive (Veni) Scheme (Grant No. 722.017.011). B.E. acknowledges The Netherlands Organization of Scientific Research (NWO) for financial support through the Innovational Research Incentive (Vidi).

■ REFERENCES

(1) Kojima, A.; Teshima, K.; Shirai, Y.; Miyasaka, T. Organometal Halide Perovskites as Visible-Light Sensitizers for Photovoltaic Cells. *J. Am. Chem. Soc.* **2009**, *131*, 6050−6051.

(2) Lee, M. M.; Teuscher, J.; Miyasaka, T.; Murakami, T. N.; Snaith, H. J. Efficient Hybrid Solar Cells Based on Meso-Superstructured Organometal Halide Perovskites. *Science* **2012**, *338*, 643−647.

(3) Yang, W. S.; Park, B. W.; Jung, E. H.; Jeon, N. J.; Kim, Y. C.; Lee, D. U.; Shin, S. S.; Seo, J.; Kim, E. K.; Noh, J. H.; Seok, S. Il. Iodide Management in Formamidinium-Lead-Halide−Based Perovskite Layers for Efficient Solar Cells. *Science* **2017**, *356* (6345), 1376−1379.

(4) Saliba, M.; Matsui, T.; Seo, J.-Y.; Domanski, K.; Correa-Baena, J.-P.; Nazeeruddin, M. K.; Zakeeruddin, S. M.; Tress, W.; Abate, A.; Hagfeldt, A.; Grätzel, M. Cesium-Containing Triple Cation Perovskite Solar Cells: Improved Stability, Reproducibility and High Efficiency. *Energy Environ. Sci.* **2016**, *9* (6), 1989−1997.

(5) Leijtens, T.; Bush, K.; Cheacharoen, R.; Beal, R.; Bowring, A.; McGehee, M. D. Towards Enabling Stable Lead Halide Perovskite Solar Cells; Interplay Between Structural, Environmental, and Thermal Stability. *J. Mater. Chem. A* **2017**, *5* (23), 11483−11500.

(6) McMeekin, D. P.; Sadoughi, G.; Rehman, W.; Eperon, G. E.; Saliba, M.; Horantner, M. T.; Haghighirad, A.; Sakai, N.; Korte, L.; Rech, B.; Johnston, M. B.; Herz, L. M.; Snaith, H. J. A Mixed-Cation Lead Mixed-Halide Perovskite Absorber for Tandem Solar Cells. *Science* **2016**, *351* (6269), 151−155.

(7) Saliba, M.; Matsui, T.; Domanski, K.; Seo, J.-Y.; Ummadisingu, A.; Zakeeruddin, S. M.; Correa-Baena, J.-P.; Tress, W. R.; Abate, A.; Hagfeldt, A.; Gratzel, M. Incorporation of Rubidium Cations into Perovskite Solar Cells Improves Photovoltaic Performance. *Science* **2016**, *354* (6309), 206−209.

(8) Rehman, W.; McMeekin, D. P.; Patel, J. B.; Milot, R. L.; Johnston, M. B.; Snaith, H. J.; Herz, L. M. Photovoltaic Mixed-Cation Lead Mixed-Halide Perovskites: Links Between Crystallinity, Photo-Stability and Electronic Properties. *Energy Environ. Sci.* **2017**, *10* (1), 361−369.

(9) Saliba, M.; Correa-Baena, J. P.; Wolff, C. M.; Stolterfoht, M.; Phung, N.; Albrecht, S.; Neher, D.; Abate, A. How to Make over 20% Efficient Perovskite Solar Cells in Regular (n-i-p) and Inverted (p-i-n) Architectures. *Chem. Mater.* **2018**, *30* (13), 4193−4201.

(10) Grancini, G.; Roldán-Carmona, C.; Zimmermann, I.; Mosconi, E.; Lee, X.; Martineau, D.; Narbey, S.; Oswald, F.; De Angelis, F.; Graetzel, M.; Nazeeruddin, M. K. One-Year Stable Perovskite Solar Cells by 2D/3D Interface Engineering. *Nat. Commun.* **2017**, *8*, 15684.

(11) Peng, J.; Wu, Y.; Ye, W.; Jacobs, D. A.; Shen, H.; Fu, X.; Wan, Y.; Duong, T.; Wu, N.; Barugkin, C.; Nguyen, H. T.; Zhong, D.; Li, J.; Lu, T.; Liu, Y.; Lockrey, M. N.; Weber, K. J.; Catchpole, K. R.; White, T. P. Interface Passivation Using Ultrathin Polymer−Fullerene Films for High-Efficiency Perovskite Solar Cells with Negligible Hysteresis. *Energy Environ. Sci.* **2017**, *10* (8), 1792−1800.

(12) Kegelmann, L.; Wolff, C. M.; Awino, C.; Lang, F.; Unger, E. L.; Korte, L.; Dittrich, T.; Neher, D.; Rech, B.; Albrecht, S. It Takes Two To Tango-Double-Layer Selective Contacts in Perovskite Solar Cells for Improved Device Performance and Reduced Hysteresis. *ACS Appl. Mater. Interfaces* **2017**, *9* (20), 17245−17255.

(13) Turren-Cruz, S.-H.; Hagfeldt, A.; Saliba, M. Methylammonium-Free, High-Performance, and Stable Perovskite Solar Cells on a Planar Architecture. *Science* **2018**, *362*, 449−453.

(14) Wu, W. Q.; Chen, D.; Caruso, R. A.; Cheng, Y. B. Recent Progress in Hybrid Perovskite Solar Cells Based on n-type Materials. *J. Mater. Chem. A* **2017**, *5* (21), 10092−10109.

(15) Correa-Baena, J. P.; Saliba, M.; Buonassisi, T.; Grätzel, M.; Abate, A.; Tress, W.; Hagfeldt, A. Promises and Challenges of Perovskite Solar Cells. *Science* **2017**, *358* (6364), 739−744.

(16) Snaith, H. J. Present Status and Future Prospects of Perovskite Photovoltaics. *Nat. Mater.* **2018**, *17*, 372−376.

(17) Lira-Cantú, M. Perovskite Solar cells: Stability Lies at Interfaces. *Nat. Energy* **2017**, *2*, 17115.

(18) Chandiran, A. K.; Abdi-jalebi, M.; Nazeeruddin, M. K.; Grätzel, M. Analysis of Electron Transfer Properties of ZnO and TiO_2 Photoanodes for Dye-Sensitized Solar Cells. *ACS Nano* **2014**, *8* (3), 2261−2268.

(19) Zhang, Q.; Dandeneau, C. S.; Zhou, X.; Cao, Q. ZnO Nanostructures for Dye-Sensitized Solar Cells. *Adv. Mater.* **2009**, *21*, 4087−4108.

(20) Özgür, Ü.; Alivov, Y. I.; Liu, C.; Teke, A.; Reshchikov, M. A.; Doğan, S.; Avrutin, V.; Cho, S.; Morkoç, H. Comprehensive Review of ZnO Materials and Devices. *J. Appl. Phys.* **2005**, *98*, 041301.

(21) Janotti, A.; Van De Walle, C. G. Fundamentals of Zinc Oxide as a Semiconductor. *Rep. Prog. Phys.* **2009**, *72*, 126501.

(22) Chen, R.; Cao, J.; Duan, Y.; Hui, Y.; Chuong, T. T.; Ou, D.; Han, F.; Cheng, F.; Huang, X.; Wu, B.; Zheng, N. High-Efficiency, Hysteresis-Less, UV-Stable Perovskite Solar Cells with Cascade ZnO−ZnS Electron Transport Layer. *J. Am. Chem. Soc.* **2019**, *141*, 541−547.

(23) Bi, D.; Boschloo, G.; Schwarzmuller, S.; Yang, L.; Johansson, E. M. J.; Hagfeldt, A. Efficient and Stable $CH_3NH_3PbI_3$-Sensitized ZnO Nanorod Array Solid-State Solar Cells. *Nanoscale* **2013**, *5*, 11686−11691.

(24) Son, D. Y.; Im, J. H.; Kim, H. S.; Park, N. G. 11% Efficient Perovskite Solar Cell Based on ZnO Nanorods: An Effective Charge Collection System. *J. Phys. Chem. C* **2014**, *118* (30), 16567−16573.

(25) Son, D. Y.; Bae, K. H.; Kim, H. S.; Park, N. G. Effects of Seed Layer on Growth of ZnO Nanorod and Performance of Perovskite Solar Cell. *J. Phys. Chem. C* **2015**, *119* (19), 10321−10328.

(26) Yang, G.; Tao, H.; Qin, P.; Ke, W.; Fang, G. Recent Progress in Electron Transport Layers for Efficient Perovskite Solar Cells. *J. Mater. Chem. A* **2016**, *4* (11), 3970−3990.

(27) Zhang, P.; Wu, J.; Zhang, T.; Wang, Y.; Liu, D.; Chen, H.; Ji, L.; Liu, C.; Ahmad, W.; Chen, Z. D.; Li, S. Perovskite Solar Cells with ZnO Electron-Transporting Materials. *Adv. Mater.* **2018**, *30*, 1703737.

(28) Zhang, H.; Cheng, J.; Lin, F.; He, H.; Mao, J.; Wong, K. S.; Jen, A. K. Y.; Choy, W. C. H. Pinhole-Free and Surface-Nanostructured NiO_x Film by Room-Temperature Solution Process for High-Performance Flexible Perovskite Solar Cells with Good Stability and Reproducibility. *ACS Nano* **2016**, *10*, 1503−1511.

(29) Nimens, W. J.; Ogle, J.; Caruso, A.; Jonely, M.; Simon, C.; Smilgies, D.; Noriega, R.; Scarpulla, M.; Whittaker-brooks, L. Morphology and Optoelectronic Variations Underlying the Nature of the Electron Transport Layer in Perovskite Solar Cells. *ACS Appl. Energy Mater.* **2018**, *1*, 602−615.

DOI: 10.1021/acsaem.9b00452
ACS Appl. Energy Mater. 2019, 2, 3736−3748

(30) Cheng, Y.; Yang, Q. D.; Xiao, J.; Xue, Q.; Li, H. W.; Guan, Z.; Yip, H. L.; Tsang, S. W. Decomposition of Organometal Halide Perovskite Films on Zinc Oxide Nanoparticles. *ACS Appl. Mater. Interfaces* **2015**, *7* (36), 19986−19993.
(31) Sin, D. H.; Jo, S. B.; Lee, S. G.; Ko, H.; Kim, M.; Lee, H.; Cho, K. Enhancing the Durability and Carrier Selectivity of Perovskite Solar Cells Using a Blend Interlayer. *ACS Appl. Mater. Interfaces* **2017**, *9* (21), 18103−18112.
(32) Janotti, A.; Van De Walle, C. G. Native Point Defects in ZnO. *Phys. Rev. B: Condens. Matter Mater. Phys.* **2007**, *76*, 165202.
(33) Trost, S.; Becker, T.; Zilberberg, K.; Behrendt, A.; Polywka, A.; Heiderhoff, R.; Görrn, P.; Riedl, T. Plasmonically Sensitized Metal-Oxide Electron Extraction Layers for Organic Solar Cells. *Sci. Rep.* **2015**, *5*, 7765.
(34) Bora, T.; Kyaw, H. H.; Sarkar, S.; Pal, S. K.; Dutta, J. Highly Efficient Zno/Au Schottky Barrier Dye-Sensitized Solar Cells: Role of Gold Nanoparticles on the Charge-Transfer Process. *Beilstein J. Nanotechnol.* **2011**, *2* (1), 681−690.
(35) Lee, D. S.; Kim, W.; Cha, B. G.; Kwon, J.; Kim, S. J.; Kim, M.; Kim, J.; Wang, D. H.; Park, J. H. Self-Position of Au NPs in Perovskite Solar Cells: Optical and Electrical Contribution. *ACS Appl. Mater. Interfaces* **2016**, *8* (1), 449−454.
(36) Carretero-Palacios, S.; Jiménez-Solano, A.; Míguez, H. Plasmonic Nanoparticles as Light-Harvesting Enhancers in Perovskite Solar Cells: A User's Guide. *ACS Energy Lett.* **2016**, *1* (1), 323−331.
(37) Kamat, P. V. Quantum Dot Solar Cells. Semiconductor Nanocrystals as Light Harvesters. *J. Phys. Chem. C* **2008**, *112* (48), 18737−18753.
(38) Wood, A.; Giersig, M.; Mulvaney, P. Fermi Level Equilibration in Quantum Dot-Metal Nanojunctions. *J. Phys. Chem. B* **2001**, *105* (37), 8810−8815.
(39) Subramanian, V.; Wolf, E. E.; Kamat, P. V. Green Emission to Probe Photoinduced Charging Events in ZnO−Au Nanoparticles. Charge Distribution and Fermi-Level Equilibration. *J. Phys. Chem. B* **2003**, *107* (30), 7479−7485.
(40) Haruta, M. Size and Support Dependency in the Catalysis of Gold. *Catal. Today* **1997**, *36*, 153−166.
(41) Liu, K.; Sakurai, M.; Liao, M.; Aono, M. Giant Improvement of The Performance of ZnO Nanowire Photodetectors by Au Nanoparticles. *J. Phys. Chem. C* **2010**, *114* (46), 19835−19839.
(42) Ruiz Peralta, M. D. L.; Pal, U.; Zeferino, R. S. Photoluminescence (PL) Quenching and Enhanced Photocatalytic Activity of Au-Decorated ZnO Nanorods Fabricated through Microwave-Assisted Chemical Synthesis. *ACS Appl. Mater. Interfaces* **2012**, *4*, 4807−4816.
(43) Chen, Z. H.; Tang, Y. B.; Liu, C. P.; Leung, Y. H.; Yuan, G. D.; Chen, L. M.; Wang, Y. Q.; Bello, I.; Zapien, J. A.; Zhang, W. J.; Lee, C. S.; Lee, S. T. Vertically Aligned {ZnO} Nanorod Arrays Sentisized with Gold Nanoparticles for Schottky Barrier Photovoltaic Cells. *J. Phys. Chem. C* **2009**, *113* (30), 13433−13437.
(44) Park, S.; Mun, Y.; An, S.; In Lee, W.; Lee, C. Enhanced photoluminescence of Au-functionalized ZnO nanorods annealed in a hydrogen atmosphere. *J. Lumin.* **2014**, *147*, 5−8.
(45) Wu, M.; Chen, W. J.; Shen, Y. H.; Huang, F. Z.; Li, C. H.; Li, S. K. In situ Growth of Match-like ZnO/Au Plasmonic Heterostructure for Enhanced Photoelectrochemical Water Splitting. *ACS Appl. Mater. Interfaces* **2014**, *6*, 15052−15060.
(46) Ehrler, B.; Musselman, K. P.; Bohm, M. L.; Morgenstern, F. S. F.; Vaynzof, Y.; Walker, B. J.; MacManus-Driscoll, J. L.; Greenham, N. C. Preventing Interfacial Recombination in Colloidal Quantum Dot Solar Cells by Doping the Metal Oxide. *ACS Nano* **2013**, *7* (5), 4210−4220.
(47) Ruf, T.; Repp, S.; Urban, J.; Thomann, R.; Erdem, E. Competing effects between intrinsic and extrinsic defects in pure and Mn-doped ZnO nanocrystals. *J. Nanopart. Res.* **2016**, *18*, 109.
(48) Qiu, W.; Ray, A.; Jaysankar, M.; Merckx, T.; Bastos, J. P.; Cheyns, D.; Gehlhaar, R.; Poortmans, J.; Heremans, P. An Interdiffusion Method for Highly Performing Cesium/Formamidinium Double Cation Perovskites. *Adv. Funct. Mater.* **2017**, *27*, 1700920.
(49) Lee, J. W.; Kim, D. H.; Kim, H. S.; Seo, S. W.; Cho, S. M.; Park, N. G. Formamidinium and Cesium Hybridization for Photo- and Moisture-Stable Perovskite Solar Cell. *Adv. Energy Mater.* **2015**, *5*, 1501310.
(50) Brillson, L. J.; Mosbacker, H. L.; Hetzer, M. J.; Strzhemechny, Y.; Look, D. C.; Cantwell, G.; Zhang, J.; Song, J. J. Surface and Near-Surface Passivation, Chemical Reaction, and Schottky Barrier Formation at Zno Surfaces and Interfaces. *Appl. Surf. Sci.* **2008**, *254* (24), 8000−8004.
(51) Brillson, L. J.; Mosbacker, H. L.; Hetzer, M. J.; Strzhemechny, Y.; Jessen, G. H.; Look, D. C.; Cantwell, G.; Zhang, J.; Song, J. J. Dominant Effect of Near-Interface Native Point Defects on ZnO Schottky Barriers. *Appl. Phys. Lett.* **2007**, *90*, 102116.
(52) Peukert, A.; Vaillant Roca, L.; Scherer, M.; Lovrincic, R.; Ramanan, C.; Chanaewa, A.; Von Hauff, E. Controlled Morphology of ZnO Nanorods for Electron Transport in Squaraine Bulk-Hetero Junction Solar Cells With Thick Active Layers. *Sol. RRL.* **2017**, *1*, 1700132.
(53) McPeak, K. M.; Le, T. P.; Britton, N. G.; Nickolov, Z. S.; Elabd, Y. A.; Baxter, J. B. Chemical Bath Deposition of ZnO Nanowires at Near-Neutral pH Conditions Without Hexamethylenetetramine (HMTA): Understanding the Role Of HMTA in ZnO Nanowire Growth. *Langmuir* **2011**, *27* (7), 3672−3677.
(54) Strano, V.; Urso, R. G.; Scuderi, M.; Iwu, K. O.; Simone, F.; Ciliberto, E.; Spinella, C.; Mirabella, S. Double Role of HMTA in ZnO Nanorods Grown by Chemical Bath Deposition. *J. Phys. Chem. C* **2014**, *118* (48), 28189−28195.
(55) Barbagiovanni, E. G.; Strano, V.; Franzò, G.; Crupi, I.; Mirabella, S. Photoluminescence Transient Study of Surface Defects in ZnO Nanorods Grown by Chemical Bath Deposition. *Appl. Phys. Lett.* **2015**, *106*, 093108.
(56) Barbagiovanni, E. G.; Strano, V.; Franzò, G.; Reitano, R.; Dahiya, A. S.; Poulin-Vittrant, G.; Alquier, D.; Mirabella, S. Universal Model for Defect- Related Visible Luminescence in ZnO Nanorods. *RSC Adv.* **2016**, *6* (77), 73170−73175.
(57) Barbagiovanni, E. G.; Reitano, R.; Franzò, G.; Strano, V.; Terrasi, A.; Mirabella, S. Radiative Mechanism and Surface Modification of Four Visible Deep Level Defect States in ZnO Nanorods. *Nanoscale* **2016**, *8* (2), 995−1006.
(58) Vempati, S.; Mitra, J.; Dawson, P. One-Step Synthesis of ZnO Nanosheets: A Blue-White Fluorophore. *Nanoscale Res. Lett.* **2012**, *7*, 470.
(59) Van Dijken, A.; Meulenkamp, E. A.; Vanmaekelbergh, D.; Meijerink, A. Luminescence of Nanocrystalline ZnO Particles: The Mechanism of The Ultraviolet and Visible Emission. *J. Lumin.* **2000**, *87*, 454−456.
(60) Azpiroz, J. M.; Infante, I.; Lopez, X.; Ugalde, J. M.; De Angelis, F. A First-Principles Study of II−VI (II 1 Zn; VI 1 O, S, Se, Te) Semiconductor Nanostructures. *J. Mater. Chem.* **2012**, *22*, 21453.
(61) Xu, H.; Dong, L.; Shi, X. Q.; Van Hove, M. A.; Ho, W. K.; Lin, N.; Wu, H. S.; Tong, S. Y. Stabilizing Forces Acting on ZnO Polar Surfaces : STM, LEED, and DFT. *Phys. Rev. B: Condens. Matter Mater. Phys.* **2014**, *89*, 235403.
(62) Winkler, S.; Frisch, J.; Amsalem, P.; Krause, S.; Timpel, M.; Stolte, M.; Würthner, F.; Koch, N. Impact of Molecular Dipole Moments on Fermi Level Pinning in Thin Films. *J. Phys. Chem. C* **2014**, *118*, 11731−11737.
(63) Lien, D. H.; Durán Retamal, J. R.; Ke, J. J.; Kang, C. F.; He, J. H. Surface Effects in Metal Oxide-Based Nanodevices. *Nanoscale* **2015**, *7* (47), 19874−19884.
(64) Shao, Y.; Xiao, Z.; Bi, C.; Yuan, Y.; Huang, J. Origin and Elimination of Photocurrent Hysteresis by Fullerene Passivation in $CH_3NH_3PbI_3$ Planar Heterojunction Solar Cells. *Nat. Commun.* **2014**, *5*, 5784.
(65) Guerrero, A.; Garcia-Belmonte, G.; Mora-Sero, I.; Bisquert, J.; Kang, Y. S.; Jacobsson, T. J.; Correa-Baena, J. P.; Hagfeldt, A. Properties of Contact and Bulk Impedances in Hybrid Lead Halide

DOI: 10.1021/acsaem.9b00452
ACS Appl. Energy Mater. 2019, 2, 3736−3748

Perovskite Solar Cells Including Inductive Loop Elements. *J. Phys. Chem. C* **2016**, *120* (15), 8023−8032.
(66) Ecker, B.; Egelhaaf, H.; Steim, R.; Parisi, J.; Von Hauff, E. Understanding S-Shaped Current-Voltage Characteristics in Organic Solar Cells Containing a TiO_x Interlayer with Impedance Spectroscopy and Equivalent Circuit Analysis. *J. Phys. Chem. C* **2012**, *116*, 16333−16337.
(67) Goossens, A.; Schoonman, J. The Impedance of Surface Recombination at Illuminated Semiconductor Electrodes. *J. Electroanal. Chem. Interfacial Electrochem.* **1990**, *289*, 11−27.
(68) Fabregat-Santiago, F.; Garcia-Belmonte, G.; Mora-Seró, I.; Bisquert, J. Characterization of Nanostructured Hybrid and Organic Solar cells by Impedance Spectroscopy. *Phys. Chem. Chem. Phys.* **2011**, *13*, 9083−9118.
(69) Walter, T.; Herberholz, R.; Müller, C.; Schock, H. W. Determination of Defect Distributions from Admittance Measurements and Application to $Cu(In,Ga)Se_2$ Based Heterojunctions. *J. Appl. Phys.* **1996**, *80* (8), 4411−4420.
(70) Chanaewa, A.; Poulsen, K.; Gräfe, A.; Gimmler, C.; Von Hauff, E. Trap-Induced Dispersive Transport and Dielectric Loss in PbS Nanoparticle Films. *Z. Phys. Chem.* **2017**, *231* (1), 121−134.

DOI: 10.1021/acsaem.9b00452
ACS Appl. Energy Mater. 2019, 2, 3736−3748